




Stability and anion diffusion kinetics of Yttria-stabilized zirconia resolved from machine learning global potential energy surface exploration

Cite as: J. Chem. Phys. 152, 094703 (2020); <https://doi.org/10.1063/1.5142591>

Submitted: 15 December 2019 . Accepted: 09 February 2020 . Published Online: 02 March 2020

Shu-Hui Guan , Ke-Xiang Zhang, Cheng Shang , and Zhi-Pan Liu 



View Online



Export Citation



CrossMark

Lock-in Amplifiers

Find out more today



 Zurich
Instruments

Stability and anion diffusion kinetics of Yttria-stabilized zirconia resolved from machine learning global potential energy surface exploration

Cite as: J. Chem. Phys. 152, 094703 (2020); doi: 10.1063/1.5142591

Submitted: 15 December 2019 • Accepted: 9 February 2020 •

Published Online: 2 March 2020



View Online



Export Citation



CrossMark

Shu-Hui Guan,^{1,2}  Ke-Xiang Zhang,² Cheng Shang,^{2,a)}  and Zhi-Pan Liu^{2,b)} 

AFFILIATIONS

¹Shanghai Academy of Agricultural Sciences, Shanghai 201403, China

²Collaborative Innovation Center of Chemistry for Energy Material, Shanghai Key Laboratory of Molecular Catalysis and Innovative Materials, Key Laboratory of Computational Physical Science, Department of Chemistry, Fudan University, Shanghai 200438, China

Note: This article is part of the JCP Special Topic on Oxide Chemistry and Catalysis.

^{a)} Email: cshang@fudan.edu.cn

^{b)} Author to whom correspondence should be addressed: zpliu@fudan.edu.cn

ABSTRACT

Yttria-stabilized zirconia (YSZ) is an important material with wide industrial applications particularly for its good conductivity in oxygen anion transportation. The conductivity is known to be sensitive to Y concentration: 8 mol. % YSZ (8YSZ) achieves the best performance, which, however, degrades remarkably under ~ 1000 °C working conditions. Here, using the recently developed SSW-NN method, stochastic surface walking global optimization based on global neural network potential (G-NN), we establish the first ternary Y–Zr–O G-NN potential by fitting 28 803 first principles dataset screened from more than 10^7 global potential energy surface (PES) data and explore exhaustively the global PES of YSZ at different Y concentrations. Rich information on the thermodynamics and the anion diffusion kinetics of YSZ is, thus, gleaned, which helps resolve the long-standing puzzles on the stability and conductivity of the 8YSZ. We demonstrate that (i) 8YSZ is the cubic phase YSZ with the lowest possible Y concentrations. It is thermodynamically unstable, tending to segregate into the monoclinic phase of 6.7YSZ and the cubic phase of 20YSZ. (ii) The O anion diffusion in YSZ is mediated by O vacancy sites and moves along the $\langle 100 \rangle$ direction. In 8YSZ and 10YSZ, despite different Y concentrations, their anion diffusion barriers are similar, ~ 1 eV, but in 8YSZ, the O diffusion distance is much longer due to the lack of O vacancy aggregation along the $\langle 112 \rangle$ direction. Our results illustrate the power of G-NN potential in solving challenging problems in material science, especially those requiring a deep knowledge on the complex PES.

Published under license by AIP Publishing. <https://doi.org/10.1063/1.5142591>

I. INTRODUCTION

The Y_2O_3 -doped ZrO_2 , also known as Y-stabilized ZrO_2 (YSZ), is a prominent family of functional and structural ceramics^{1–6} with many crystal structures, e.g., the monoclinic phase at low Y concentrations and the tetragonal or cubic phase at high Y concentrations.^{7,8} Among them, the cubic phase (fluorite structure) is most used, particularly as oxygen sensors and catalysts in fuel/electrolysis

cells for its high oxygen anion conductivity. The role of doping Y, the element with a larger ionic radius and a lower valency compared to Zr, is known not only to stabilize the cubic structure by cation substitution, but also to introduce anion vacancies (O_v) for allowing oxygen diffusion.^{9,10} It is found that the 8 mol. % Y (8YSZ) achieves the highest conductivity,^{11–15} which, however, drops remarkably^{16–18} within less than 1000 h under the 1000 °C working condition. Despite extensive studies in the past 35 years, it remains elusive

why the highest conductivity occurs at 8YSZ, instead of those with higher Y concentrations that should contain more O_v and what is the origin for the rapid drop in the ionic conductivity of 8YSZ. Both questions are critical for the design of new materials with better performances.

One of the key challenges in the field is to determine the atomic structure of YSZ, especially for low Y concentration YSZ, i.e., to characterize where the Y and O_v reside in the lattice. Taking 8YSZ as an example, there is an astronomically large number of possible configurations in a 316-atom cube (a $3 \times 3 \times 3$ ZrO_2 cubic supercell): 108 cation sites (92 Zr and 16 Y) and 216 anion sites (208 O and 8 O_v) allow $C_{108}^{16} \times C_{216}^8 = 5.55 \times 10^{42}$ permutations. It is, therefore, no wonder that even some simple questions, e.g., whether O_v prefers to reside near Y,^{19–24} remains not concluded. While most studies indicate that the vacancy favors to bind with the host Zr cations until the Y level above 40 mol. %, ^{25–27} a recent study by Kawata²⁸ also found that at the Y concentration level as low as 10 mol. %, the O_v near Y as the nearest neighbors (1NN) is also evident according to the nuclear magnetic resonance (NMR) spectrum.

Because of the structural uncertainty of YSZ systems, the debate on the mechanism for the conductivity peak at 8YSZ continues for three decades. Two popular mechanisms were proposed in the literature to account for the decrease in conductivity above 8 mol. %. (i) The increase in vacancy concentration leads to the ordering/clustering of O_v that inhibits the diffusion of oxygen. Using neutron and x-ray diffraction analysis, Goff *et al.*²⁹ found that the O_v preferentially arrange along the $\langle 111 \rangle$ direction below ~ 15 YSZ and as the Y concentration increases, these $\langle 111 \rangle$ vacancy pairs pack together in $\langle 112 \rangle$ directions to form aggregates. Later molecular dynamics (MD) simulations by Marrocchelli *et al.*^{30,31} confirm that the $\langle 111 \rangle$ arranged O_v is beneficial to the O diffusion, although their theoretical models have Y concentrations of at least 9.6 mol. %. (ii) The increase in Y–O–Y and Y–O–Zr local structure patterns at elevated Y concentrations inhibits the O anion diffusion. Several theoretical calculations showed that the O_v diffusion following the path along the Zr–Zr edge has a much lower reaction barrier (~ 0.6 eV) compared to those along Y–Y (1.8 eV) or Y–Zr (1.2 eV) edges.^{32,33} By using isotope ^{18}O tracer, Kilo *et al.*³⁴ measured the activation energy for O_v diffusion in YSZ with Y concentrations ranging from 8 mol. % to 24 mol. % at 650–1200 K, and found that the activation energy is rather constant, ~ 1 eV. The inhibition effect was attributed to the decrease in the Zr–O–Zr pattern concentration along the O_v diffusion pathway. However, this constant activation energy is not consistent by theoretical studies by a number of groups, who predicted that the activation energy has a nearly linear increase with the increase in the concentrations.^{35–37} A possible explanation is the initial structures utilized in modeling might not correspond to the realistic structure in the experiment.

Furthermore, the origin for the decrease in conductivity with aging is also highly controversial. By observing the microstructure evolution using selected area electron diffraction (SAED) and transmission electron microscopy (TEM) techniques, Butz, *et al.*¹⁵ found that the tetragonal precipitates grow during the aging process from about 1 nm up to approximately 15 nm in 8YSZ at 950 °C and, thus, suggests that the phase transformation from cubic to tetragonal reduces the conductivity. The similar idea was also suggested by several other groups.^{16,17} On the other hand, Kondoh *et al.*,^{38–40} by using extended x-ray absorption fine structure (EXAFS), observed

the decrease in the 1NN coordination number of Zr ions (from 8 to 5.6) in the aging experiment of 8YSZ, and suggests that the short range ordering of O_v occurs. The O_v aggregation may explain the decrease in conductivity.

The above puzzles can be generalized as the problems related to the great complexity of the PES in the Y–Zr–O system. The traditional PES sampling techniques such as MD simulation, often start from a pre-guessed configuration and, due to the limited time scale, e.g., normally < 5 ns, are frustrated to reveal the rare events on the structural phase transition, including the cation diffusion, the O_v aggregation, and the aging of 8YSZ occurred in reality. It does not even mention that the empirical force field potentials^{41–46} utilized in these simulations are known to predict incorrectly the ordering for low energy states in YSZ, as benchmarked against first principles calculations.

Here, we aim to provide deeper insights into the microstructure of YSZ at different Y concentrations by using the recently developed machine learning based global PES exploration technique, namely stochastic surface walking^{47,48} global exploration with global neural network potential (SSW-NN).^{49–51} We construct the first Y–Zr–O ternary global NN (G-NN) potential, establish the thermodynamic convex hull diagram for YSZ with Y concentrations from 5.3 mol. % to 40 mol. % and identify the atomic structure for the most stable phase, the so-called global minimum (GM), at each Y concentration. The long-standing puzzles on the stability and the conductivity of YSZ are, thus, resolved from our thermodynamics and kinetics data.

II. METHODOLOGY AND CALCULATION DETAILS

All simulations based on neural network potential were carried out by using our recently developed LASP software,⁵² Large-scale Atomic Simulation with neural network Potential (webpage www.lasphub.com), which implements the data-generation using SSW global optimization,^{47,48} training, and evaluation of G-NN potentials.⁴⁹ In addition to G-NN functionalities, LASP provides various interfaces to the common first principles density functional theory (DFT) packages as well as multiple modules (e.g., SSW) for PES exploration. The methodology of SSW global optimization and reaction sampling (SSW-RS) has been detailed previously and also introduced in the [supplementary material](#), part 1. Here, we will review briefly the procedure to construct the global NN potential for the Y–Zr–O ternary element system, and benchmark our G-NN calculations with DFT and force field calculations.

The ternary Y–Zr–O G-NN potential is obtained by self-learning of the SSW global PES dataset that covers a wide range of $Y_{2x}Zr_{1-2x}O_{2-x}$ compositions with different structural types (e.g., bulks, surfaces, and clusters). The dataset is calculated by plane-wave DFT calculations as implemented in VASP (Vienna Ab-initio Simulation Package)⁵³ at the high accuracy setups (see below). The typical procedure and the hyperparameters utilized in G-NN training can be found in our recent publications.^{52,54} Specifically, more than 10^7 structures on $Y_{2x}Zr_{1-2x}O_{2-x}$ global PES were visited by SSW-NN during NN potential generation and the final training dataset of $Y_{2x}Zr_{1-2x}O_{2-x}$ consists of 28 803 structures that are selected to represent the global PES. The G-NN follows the feed-forward NN architecture with five-layers (188-60-50-50-1) for each element, reaching 71 103 fitting parameters in total.^{52,54} The details

on the training dataset are shown in the [supplementary material](#), Table S1, which covers pure Zr, ZrO_x , Y_2O_3 , and $Y/Zr \sim 1:9$ to $\sim 4:3$ mixed oxides. For the final G-NN potential, the root-mean-square (RMS) errors for the energy and the force reach 7.674 meV/atom and 0.165 eV/Å, respectively. This G-NN potential is now included in the G-NN library of LASP⁵² (accessible from LASP webpage, www.lasphub.com). We have also benchmarked the G-NN accuracy against the DFT results for important structures, which shows that the energy RMS is 1.38 meV/atom for the low energy structures and pathways in this work (see the [supplementary material](#), Table S2). This small error suggests that the G-NN PES is a good approximation to DFT PES and can be utilized to expedite the global structure search and pathway determination.

The G-NN potential training relies on the DFT calculated energy, forces, and stresses of structures.^{52,54} To achieve the high accuracy and the data consistency, our DFT calculations in VASP utilize the following standard setups in LASP G-NN library generation: DFT functional at the level of generalized gradient approximation (GGA-PBE);⁵⁵ the kinetic energy cutoff being 450 eV; the projector augmented wave (PAW) pseudopotential⁵⁶ to describe ionic core electrons; the fully automatic Monkhorst–Pack K-mesh with 25 times the reciprocal lattice vectors⁵⁷ for the first Brillouin zone k -point sampling.

For interests, we also benchmarked the results using G-NN, the force–field potential where the ion–ion interaction is described by the Buckingham potential⁴² and the Coulombic potential, and DFT calculations. We compared the energy of five low energy structures of 8YSZ and the results are listed in the [supplementary material](#), Table S3. It shows that the energy error between empirical potential and DFT reaches ~ 10 meV/atom, while the energy error is within 1.7 meV/atom between G-NN potential and DFT. In addition, the force–field potential finds the wrong GM and yields the wrong energy ordering.

All the transition states (TS) are searched using double-ended surface walking method (DESW). The DESW method⁵⁸ operates with two structural images starting from the reactant and the product, respectively, to walk step wisely toward each other. The surface walking involves the repeated bias potential addition and local relaxation with the biased-CBD method to correct the walking direction, in a manner similar to the SSW⁴⁷ and BP-CBD methods.⁵⁹ The identified TS structure will finally be retrieved using the Gonzalez–Schlegel IRC method⁶⁰ by extrapolating the TS structure toward the reactant and the product. The TS is confirmed via the phonon analysis with one and only one negative frequency.

III. RESULTS

A. Thermodynamics convex hull and GM structures of YSZ

Our investigations start from the phase space scan for bulk $Y_{2x}Zr_{1-2x}O_{2-x}$ structures with eight different Y concentrations ($Y_2O_3\% = Y_2O_3/(Y_2O_3 + ZrO_2) = x/(1-x) = 5.3\%$, 6.7%, 8.0%, 10.0%, 14.3 mol. %, 20.0 mol. %, 33.3 mol. %, and 40.0 mol. %) using the SSW-NN method. For each composition, we generally run in parallel a number of SSW-NN search, where more than 40 000 minima are visited using different supercells up to 316 atoms per cell (the supercell size for each composition studied are detailed in the [supplementary material](#), Table S4). From these global PES data, the GM

is, thus, obtained for each composition (all structure coordinates listed in the [supplementary material](#)).

Taking the energetics of GM, we can plot the thermodynamic convex hull for $Y_{2x}Zr_{1-2x}O_{2-x}$, as shown in [Fig. 1\(a\)](#), where the relative formation energy (ΔE) of $Y_{2x}Zr_{1-2x}O_{2-x}$ is plotted against $Y_2O_3\%$. The ΔE is defined in Eq. (1), which is the energy per O anion with respect to the bulk Y_2O_3 and ZrO_2 (both in the cubic phase). It should be mentioned that the GM of 5.3 mol. % is +7 meV per O anion less stable than the pure phases and, thus, not shown in [Fig. 1\(a\)](#),

$$\Delta E = \frac{E_{Y_{2x}Zr_{1-2x}O_{2-x}} - (xE_{Y_2O_3} + (1-2x)E_{ZrO_2})}{2-x}. \quad (1)$$

It is obvious that the diagram has three convex points at 6.7 mol. %, 20 mol. %, and 40 mol. %, i.e., 6.7YSZ, 20YSZ, and 40YSZ. The convex points in the convex hull diagram are the thermodynamic stable phases, where the phase segregation to the neighboring phases is not favored thermodynamically. We note that the most concerned 8YSZ is not a convex point, indicating that the phase segregation from 8YSZ to the neighboring 6.7YSZ and 20YSZ is exothermic. Indeed, this energy is calculated to be -12 meV per anion.

By inspecting the GM structures, we found that with the increase in $Y_2O_3\%$, more Y atoms replace the Zr positions and the GM of YSZ becomes more cubic like. This can be seen clearly from the simulated x-ray diffraction (XRD) patterns for the GM structure at each composition. As shown, 6.7YSZ is a typical monoclinic phase with the major peaks (2θ) at 27.5° , 31.1° , 34.1° , 40.1° , 49.1° , and 53.2° , which correspond to the crystal plane indices of $(11\bar{1})$, (111) , (002) , $(21\bar{1})$, (220) , and (300) of the monoclinic ZrO_2 . With the increase in $Y_2O_3\%$, the monoclinic $(21\bar{1})$ and (300) peaks at $2\theta = 40.1^\circ$ and 53.2° disappear, and the monoclinic $(11\bar{1})$ and (111) peaks at $2\theta = 27.8^\circ$ and 31.1° merge gradually to one (111) peak at $2\theta = 29.5^\circ$ of the cubic phase, which is the characteristic peak in cubic symmetry. The phases in between 6.7% and 20% are distorted cubic phases and above 20%, the YSZ exhibit the clean cubic phase characteristics.

In fact, for 33.3YSZ and 40YSZ, they are new ordered phases, namely, $Zr_2Y_2O_7$, a cubic pyrochlore structure (FD-3M, No. 227) for 33.3YSZ and $Zr_3Y_4O_{12}$, a rhombohedral structure (R-3, No. 148) for 40YSZ named δ phase in the experiment. We note that the experiment⁷ has shown that as early as $\sim 20\%$ Y concentration, the δ phase (40YSZ) starts to appear. This, in fact, also suggests that the structure with Y concentration in between 20% and 40% are thermodynamically unstable, which agrees with the prediction from our convex hull. For the low Y concentration below 20%, both monoclinic and cubic phases are observed in the experiment, again in agreement with the dual convex points at 6.7% (a monoclinic phase) and at 20% (distorted cubic phase) from the theory.

B. O_v distribution in YSZ

For the importance of O_v to the conductivity of YSZ, we have analyzed the O_v distribution in the GM structures for Y concentrations above 8%. The O_v in these cubic structures can be identified readily; its position is defined numerically as the center of the tetragonal void surrounded by four neighboring cations. In [Fig. 2](#), we plot the radial distribution functions (RDF), $g(r)$, for $Zr-O_v$, $Y-O_v$, and

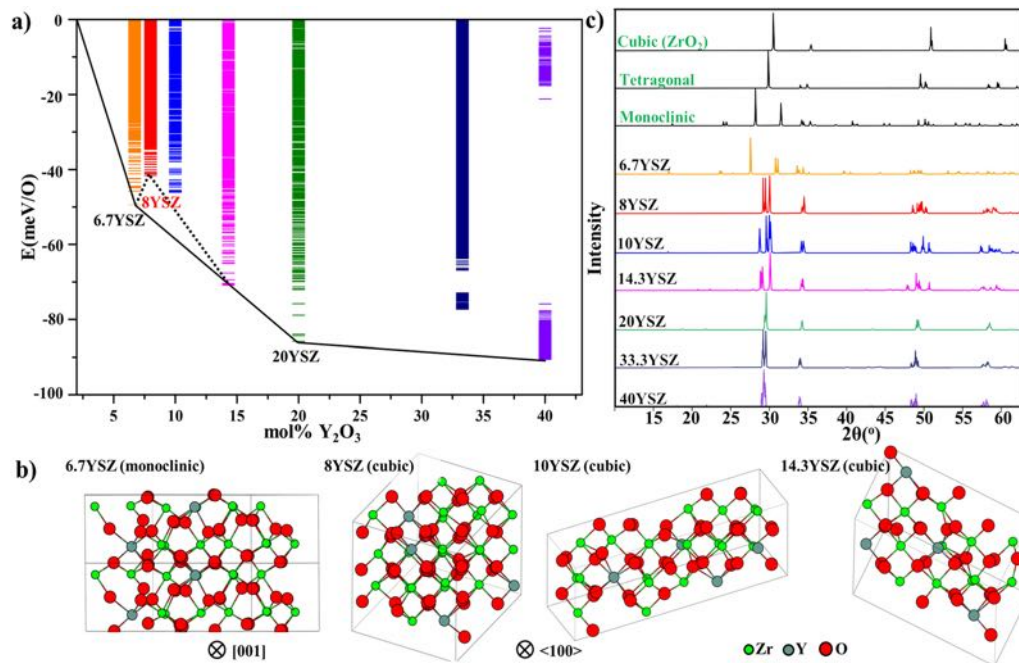


FIG. 1. (a) Thermodynamic convex hull diagram for $Y_{2x}Zr_{1-2x}O_{2-x}$ with respect to the cubic- ZrO_2 and cubic- Y_2O_3 (as the energy zero). The energy spectrum for low energy structures in each composition is shown as the color bars. (b) The atomic structures of four GMs at low Y concentrations. (c) Simulated x-ray diffraction patterns of the GM structures that are compared with the standard ZrO_2 phases.

O_v-O_v pairs (in fact, we have also plotted $g(r)$ for Zr-O and Y-O pairs, and because they are quite similar to those of Zr- O_v and Y- O_v , they are only shown in in Fig. S2). The $g(r)$ is computed as

$$g_{X-O_v}(r) = \frac{V}{N_{O_v}} \frac{\frac{1}{N_X} \sum_{i=1}^{N_X} n_{O_{v,i}}}{4\pi r^2 \Delta r}, \quad (2)$$

where X represents the centering Zr, Y, or O_v ; $n_{O_{v,i}}$ is the number of O_v situated in between the distance r to $r+\Delta r$ from the centering X atom. All $g(r)$ has been normalized by dividing the total number of centering atom, the number of anionic sites N_{O_v} in the perfect cubic lattice ($= N_o + N_{O_v}$), and the volume of the cell (V).

The RDFs of Zr- O_v and Y- O_v in Fig. 2 show that the cation- O_v peaks appear at the similar positions, i.e., 2.2–2.5 Å for the first O_v -cation peak, 4.1 Å for the second, and so on. This implies that Y- O/O_v and Zr- O/O_v distances are close, and thus, Y/Zr is exchangeable. However, at the different Y concentrations, the relative magnitude and the distribution of the Zr- O_v and Y- O_v peaks differ. In particular, one can see that the first Y- O_v peak at 2.3 Å start to appear above 20YSZ and increase further in intensity in 40YSZ. This indicates clearly that the O_v avoids to be the 1NN of Y cations until the high Y (20%) concentration.

In addition, we also examined the cation-O RDFs (shown in Fig. S3) and found that these RDFs are similar with each other, irrespective of the Y concentration. We note that the first peak of the Zr-O pair (~2.2 Å) appears slightly earlier than that of the Y-O pair (~2.4 Å), consistent with the general knowledge that the Zr cation radius is smaller than the Y cation radius. From the RDF of both

cation- O_v and cation-O pairs, we cannot identify obvious difference between 8YSZ and other YSZs.

For the RDF of O_v-O_v pairs (Fig. 2), the distributions are more complex, and 8YSZ now exhibits distinct features. In 8YSZ, the first O_v-O_v peak appears at a long distance ~5.8 Å, which is along the $\langle 210 \rangle$ crystallographic direction, and the second O_v-O_v peak is at 8.8 Å along the $\langle 222 \rangle$ direction (note that $\langle 222 \rangle$ is in the same direction as $\langle 111 \rangle$ but the separation is doubled in space). There is a large empty gap in between 5.8 Å and 8.8 Å. We note that other YSZs (10YSZ to 40YSZ) generally have more homogeneous distribution in O_v , particularly at high Y concentrations. They all have the O_v-O_v peak at 6.2 Å, which is along the $\langle 112 \rangle$ direction, but have very low (or zero) intensity at the $\langle 222 \rangle$ direction. In particular, a very strong $\langle 112 \rangle$ intensity appears at both 20% and 40%, the two convex points, which indicates the preferential alignment of O_v along this direction at high Y concentrations. Only at the highest Y concentrations, 33.3% and 40%, the shortest distance O_v-O_v peak occurs at 4.4–4.8 Å, which is an indication of $\langle 111 \rangle$ and $\langle 200 \rangle$ alignments, where two O_v s appear in the 1NN shell of the same cation, e.g., O_v-Zr-O_v in six-coordinated Zr.

C. Global PES of 8YSZ

Since our bulk thermodynamics data suggests that 8YSZ is not thermodynamically stable, we have examined in detail the global PES of 8YSZ. We collected the global PES data for 8YSZ, where more than 80 000 minima visited by extensive SSW-NN search with three different supercells, i.e., the 79-atom, 158-atom, and 316-atom supercells. After removing the duplicate minima (e.g., permutation

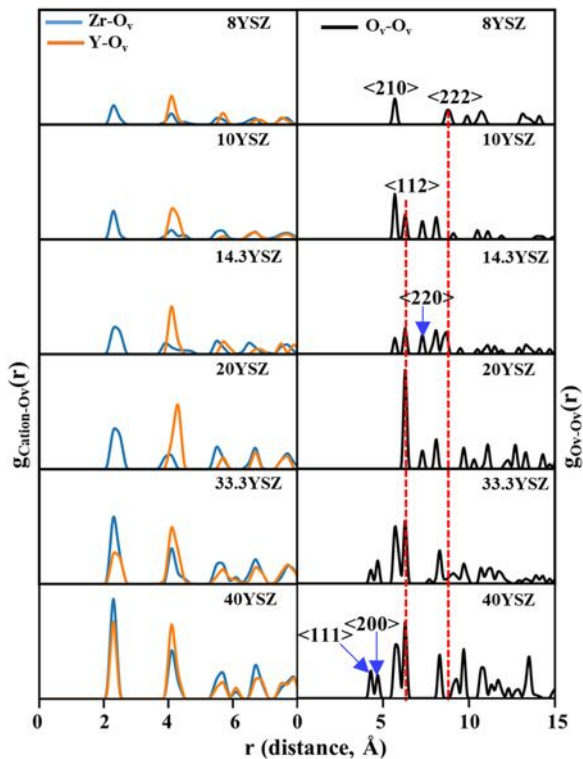


FIG. 2. Radial distribution function $g(r)$ of the cation- O_v (left panel) and O_v - O_v (right panel) pairs in the GMs of YSZs at different Y concentrations.

isomers), we finally obtain 25 907 distinct minima, including both crystals and amorphous structures. To visualize these structures, we project them on a two-dimensional structure fingerprint—energy contour plot in Fig. 3(a). The structure fingerprint (x-axis) utilizes the distance-weighted Steinhardt order parameter⁶¹ with the degree $l = 4$ (OP_4) (also see the supplementary material for details) that is found to best distinguish different structures. The color scheme, from red to blue, is utilized to indicate the density of states (DOS) of the structural minimum. As there are already a substantially large number (2032) of distinct minima below 80 meV per O, we focus on the enlarged global PES plot in the 0–80 meV energy window and the plot of the whole energy range is shown in the inset.

To understand the global PES structures, we also calculated the average coordination numbers of cations in the 1NN bonding shell and the next nearest neighbor (2NN) bonding shell. The average of coordination numbers (\overline{CN}) is defined as

$$\overline{CN}(X) = \frac{\sum_{i=1}^{N_X} n_{O_i}}{N_X}, \quad (3)$$

where X represents Zr or Y; n_{O_i} is the number of oxygen atoms situated in 1NN or 2NN of X; and N_X is the number of X cations in the cell. As a reference, in cubic ZrO_2 $\overline{CN}(Zr) = 8$ for the 1NN shell and $\overline{CN}(Zr) = 24$ for the 2NN shell.

Figure 3(a) shows that the GM of 8YSZ has close energy with many other cubic minima, i.e., more than ten distinct minima within 12 meV per O. The nearly degeneracy in energy also suggests that

8YSZ has a smooth PES and can be a mixture of different local structure patterns at high temperatures.^{62,63} We marked six representative low energy minima with black dots and triangle in Fig. 3(a), namely GM, Str-1 to Str-6 from low to high in energy, which are all cubic lattice structures but with different distribution for Y cations and O_v . Four of them, i.e., GM, Str-1, Str-4, and Str-5, are highlighted in Fig. 3(b) and two (Str-2 and Str-3) are shown in Fig. S2 for their similarity with Str-1.

For the lowest energy minima (GM, Str-1, Str-2, and Str-3), they are very similar in structure (as shown in the RDF of cation- O_v , O_v - O_v , and Y-Y in Fig. S4). In all these minima, all O_v locates at the 2NN of Y with an O_v -Y distance being at least 4.2 Å. The calculated $\overline{CN}(Y)$ is 8.0 at the 1NN and ~ 22.4 at the 2NN. The O_v distributions of these structures are compared in Fig. S4, which shows that all the O_v distribute along $\langle 210 \rangle$ and $\langle 222 \rangle$, but not along $\langle 112 \rangle$, which are the same as that in GM (Fig. 2). The Y distribution is the main difference between minima and elaborated below.

GM: The Y cations are paired in the GM [Fig. 3(b)] with the shortest Y-Y distance being 3.7 Å and the pair-pair distance being at least 6.3 Å. The Y distribution align along $\langle 110 \rangle$, as seen from the main peak in the RDF of Y-Y (see the supplementary material Fig. S4).

Str-1: It is 1.9 meV per O above GM. Four Y cations connect in a “Z” shape and the Y_4 cluster is at least 6.5 Å away from the other Y_4 cluster. Similarly, the Y cations align in the $\langle 110 \rangle$ direction.

Str-2 and Str-3: They are 4.9 meV and 6.5 meV above GM, respectively. For Str-2, three Y cations form a triangle shape, which is at least 6.3 Å away from a single Y cation. The Y_3 triangle locates in the $\{111\}$ plane. For Str-3, four Y cations distribute homogeneously in the cell without the Y-O-Y connection. The Y distribution no longer aligns along $\langle 110 \rangle$ and the shortest Y-Y distance is 5.1 Å.

Further increasing the energy, we note that the O_v distribution becomes different. For Str-4 and Str-5, which are 8.5 meV and 11.9 meV per O above GM, they start to have the $\langle 112 \rangle$ peak in O_v - O_v RDFs. On the other hand, the Y cations of them are also paired, the same as GM structures with the shortest Y-Y distance being 3.7 Å and the pair-pair distance being 6.3 Å. All O_v still locates at the 2NN of Y.

About 20 meV per O above from GM, the global PES enters into a large DOS zone, where many energy degenerate structures are present. These structures are generally cubic-like structures, but locally with the features of the monoclinic phase [We can distinguish the monoclinic phase according to (i) the local $CN(Zr)$ at 1NN drops to 7 and (ii) the appearance of $2\theta = 28^\circ$ and 31° in the simulated XRD pattern]. We show two such typical structures in this zone in the supplementary material Fig. S2, as indicated by the red dot in Fig. 3(a). From the global PES, it is unlikely that 8YSZ can transform uniformly to the monoclinic phase due to the high energy cost.

We can now summarize some key findings on the structures of YSZ as follows: YSZ adopts the monoclinic crystal structure below 8% and the cubic structure above 8%. The most concerned 8YSZ is thermodynamically unstable and the phase segregation into the 6.7YSZ and 20YSZ is exothermic by 12 meV per O atom. In 8YSZ, Y cations tend to form Y-O-Y pairs and the homogeneous distribution of the Y cation is less stable by at least 6.5 meV per O atom. The O_v prefers to locate at the 2NN of Y and align along $\langle 210 \rangle$ and $\langle 222 \rangle$ directions. The structure with O_v along the $\langle 112 \rangle$ direction is less unstable by at least 8.5 meV per O atom. The O_v distribution

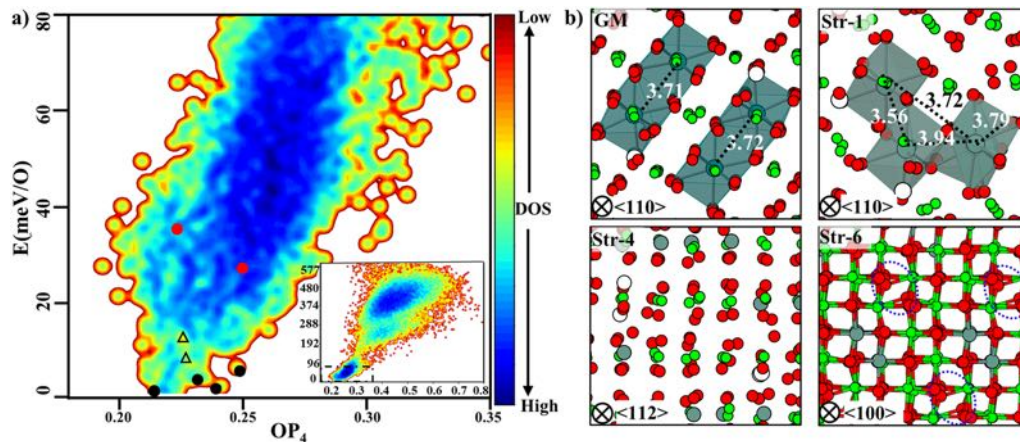


FIG. 3. (a) Global PES for low energy structures using the $OP_4 \sim E$ contour plot that is enlarged from the same plot in the inset covering the full energy range from the SSW-NN PES data. OP_4 : the structure order parameter with $l = 4$. Some representative structures mentioned in the text are labeled by black/red dots and triangles, and their coordinates (OP_4 , E) are listed: black dots: GM (0.217, 0.00); Str-1 (0.242, 1.9); Str-2 (0.234, 4.9); Str-3 (0.248, 6.5); black triangles: Str-4 (0.225, 8.5); Str-5 (0.224, 11.9); and red dots: Str-6 (0.243, 29.8), and Str-7 (0.222, 34.7). (b) Atomic structures of GM, Str-1, Str-4, and Str-5, showing different Y and O_v distributions. The shaded polyhedron indicates the Y coordination. The distance labeled is in Å. The dotted circles in Str-6 indicate the local pattern of the monoclinic phase characteristics. Y: dark-green ball; Zr: green ball; O: red ball; and O_v : white ball.

in 8YSZ is distinct from YSZs with higher Y concentrations, which generally have O_v aligned along the $\langle 112 \rangle$ direction.

It is of significance to discuss our theoretical findings in the context of previous experimental observations. On the structural aspects, two key information on O_v were often referred to in the experiment, i.e., the O_v -cation relationship and the O_v distribution. From the identified GM for different YSZs, we show that O_v has a strong tendency to locate only the nearby Zr cation as the 1NN until 33.3YSZ, and appear as the 2NN to the Y cation as early as 8YSZ. While most experimental observations do confirm the O_v preference with Zr, one ^{89}Y MAS NMR experiment detected O_v near Y at Y concentrations above 10 mol. %. We, however, note that the experiment was performed by sintering samples at high temperature (1600 °C), a temperature much higher than the typical working temperature of YSZ (~ 1000 °C). Our global PES data indicate that the energy difference between the two structural patterns, i.e., Y- O_v and Zr- O_v in the 1NN position, is not large, within 9 meV per O in 14.3YSZ and 20YSZ. The increased configurational entropy at high temperatures should be responsible for the observation of the Y- O_v pattern.

As for O_v distribution, we show that O_v sites tend to avoid each other, i.e., the O_v - O_v distance is at least ~ 4.8 Å. This fact leads to that the O_v distribution prefers $\langle 210 \rangle$ and $\langle 222 \rangle$ at 8YSZ, but shifts to $\langle 112 \rangle$ at higher Y concentrations. Indeed, the experiment by Goff²⁹ observed the O_v aggregates in $\langle 112 \rangle$ directions with the increase in Y concentrations. The O_v - O_v and O_v -Y repulsion play critical roles in the O_v diffusion kinetics, as identified in Sec. III D.

D. O anion diffusion in 8YSZ and 10YSZ

To provide deeper insights into the unique high conductivity of 8YSZ, we have investigated the anion diffusion kinetics in 8YSZ and 10YSZ by examining the lowest energy pathway of anion migration mediated by O_v sites. Our calculations for finding

diffusion pathways focused on the GM configuration that should have the largest population from statistics, and adopted large supercells to avoid the O_v interaction with its images, i.e., 158-atom supercell for 8YSZ and 128-atom supercell for 10YSZ. The SSW reaction pathway sampling^{47,48} (SSW-RS, also see the [supplementary material](#) for details on methodology) was utilized to sample the likely pathways by tracking the disappearance of O_v from its original position at the GM. Specifically, our SSW-RS starts from GM of 8YSZ or 10YSZ, defined as the initial state (IS), and explore exhaustively the likely structures nearby (>5000 minima), defined as the final states (FS), until a significant number of IS/FS pairs (>300) were collected. The pathways between all these IS/FS pairs can then be established facilely by using the DESW method to locate the TS, and the reaction barriers can, thus, be determined. Because of the different chemical environment of vacancy, the reaction barrier of vacancy migration determined from more than 300 different pathways (397 for 8YSZ and 683 for 10YSZ) spans in a window, which is 0.96–1.15 eV for 8YSZ and 0.95–1.69 eV for 10YSZ. For comparison, in the following, we focused on the lowest energy barrier pathway for the vacancy diffusion in the GM configuration.

In Table I, we summarized the main results from the lowest energy pathways for 8YSZ and 10YSZ. Two lowest energy pathways in 8YSZ involve O_v diffusion to the 2NN positions labeled 8-P1 and 8-P2. Because O_v in 10YSZ can only diffuse to the 1NN position in the lowest energy pathways (labeled 10-P1 and 10-P2), we also listed the lowest energy pathways to the 2NN positions for comparison, labeled 10-P3 and 10-P4. From these pathways, we found that (i) not surprisingly, no cation movement occurs, indicating that the cation movement is kinetically unlikely; (ii) the O_v diffusion generally occurs along $\langle 100 \rangle$ directions, apparently because the O anions at these directions are the closest to the O_v site (1NN position, ~ 2.5 Å) in the cubic lattice.

For 8YSZ, both lowest energy pathways involve the O_v diffusion directly to the 2NN position, with the overall distance of anion

TABLE I. Lowest energy pathways for the anion diffusion in 8YSZ and 10YSZ.^a

Species	Pathway	E_a	ΔE	Distance
8YSZ	8-P1	0.96	0.79	3.6
	8-P2	1.15	1.06	3.6
10YSZ	10-P1	0.96	0.69	2.5
	10-P2	1.15	0.95	2.5
	10-P3	1.57	1.43	3.6
	10-P4	1.69	1.61	3.6

^aListed data include the O_v diffusion reaction barrier (E_a , eV), the energy difference between the FS and the GM structure (ΔE , eV), and the overall distance of anion diffusion with respect to GM (Distance, Å).

migration being 3.6 Å. The reaction barrier of the diffusion is 0.96 eV and 1.15 eV and the reactions are endothermic by 0.79 eV and 1.06 eV considering that the FS structures deviate from the GM. On the other hand, in the lowest energy pathways of 10YSZ, the O_v can only diffuse to its 1NN position with the overall distance for anion migration being 2.5 Å. The reaction barriers are close to those in 8YSZ, being 0.96 eV and 1.15 eV. Interestingly, the diffusion to the 2NN position in 10YSZ is kinetically more difficult, requiring a much higher overall barrier, up to 1.69 eV (see Table I). The high barrier is consistent with the highly unstable nature of the FSs, which are up to 1.61 eV more unstable compared to the GM. Therefore, the key difference between 8YSZ and 10YSZ lies in the diffusion distance in the lowest energy pathways. Apparently, significant repulsion interactions are present in 10YSZ to restrict the anion diffusion.

By closely inspecting these pathways, we can understand how oxygen anions migrate as mediated by O_v sites. As the representative, in Fig. 4, we illustrate the low energy pathways for 8-P2 diffusion in 8YSZ. This is an elementary reaction involving two oxygen atoms cooperative movements, labeled 1 and 2 in figure. In the reaction, oxygen 1 that coordinates with Y first moves along the [100] direction to fill the neighboring O_v . As a result, an O_v appears near Y at the TS, the pattern that is known to be unstable from our global PES data. Next, a nearby oxygen 2 that coordinates only with Zr shifts to this newly formed O_v site along the [001] direction. Finally, an O_v site appears at the site initially occupied by oxygen 2, leading to an overall distance of 3.6 Å for O diffusion to a 2NN position

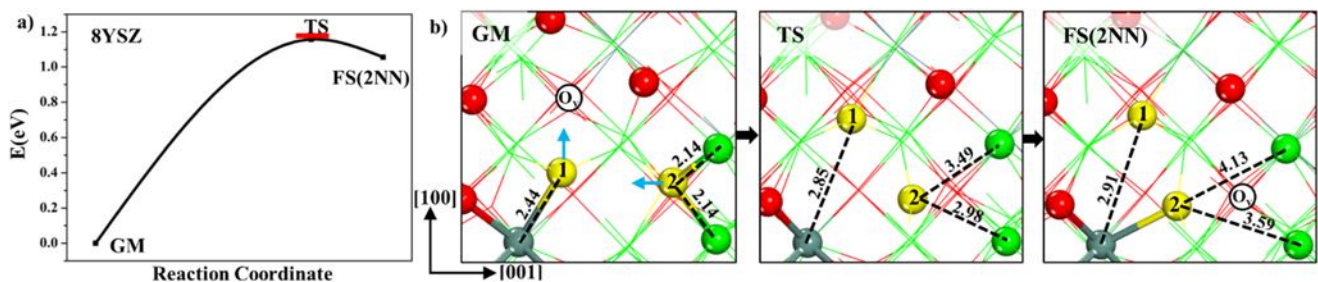


FIG. 4. (a) The energy profile for the lowest energy pathway (8-P2) of the anion diffusion in the GM of 8YSZ. (b) Snapshots of the structures along the pathway shown in (a). The distance labeled is in Å. Y: dark green ball; Zr: green ball; and O/reacting O: red/yellow balls.

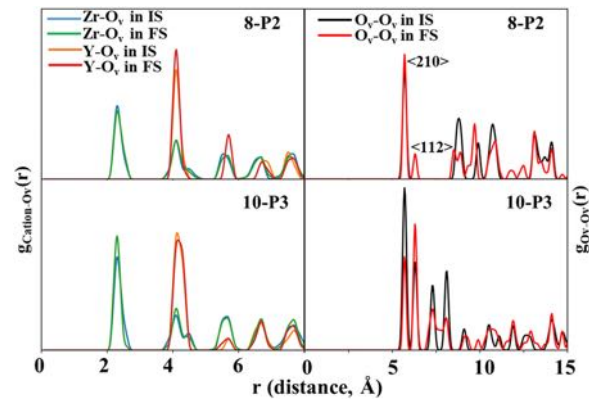


FIG. 5. Radial distribution function $g(r)$ of the cation- O_v (left panel) and O_v - O_v (right panel) pairs in the IS and FS of the pathway 8-P2 (8YSZ) and the pathway 10-P3 (10YSZ).

along the [101] direction. It can also be seen from Fig. 5 that plots the RDF of cation- O_v and O_v - O_v from IS to FS. We note that O_v becomes more homogeneously distributed at the FS with several additional peaks. In particular, the $\langle 112 \rangle$ peak that originally is not present in the GM of 8YSZ now has a small intensity.

We would like to emphasize that despite the difference in diffusion distance, the oxygen anion diffusion in 10YSZ behave similarly as those in 8YSZ. In all cases, the diffusion is along the $\langle 100 \rangle$ direction, where an O anion at the 1NN position to the O_v migrates to fill the O_v . To migrate to the 2NN, two O anions are involved, first along [100] and second along [001], resulting in the net movement of O_v along [101].

It is important to understand why the O anion diffusion to the 2NN positions is frustrated in 10YSZ. To this end, we have compared the geometrical features of the FS structures since the FS of the O_v diffusion to the 2NN position (10-P3 and 10-P4 in Table I) are highly unstable compared to its GM in 10YSZ. As also shown in Fig. 5, we found that compared to the GM, the Zr cations in the FSs of 10YSZ gets closer to the O_v , as reflected by the first peak intensity increase in the Zr- O_v RDF. By contrast, there is no significant change in Zr- O_v RDF in the FS of 8YSZ. This implies that the redistribution of O_v in 10YSZ leads to the closer contact of Zr- O_v , which destabilizes the FS structures.

With this knowledge, the difficulty of O anion migration in 10YSZ can now be understood as follows. Our global PES data show that the O_v distribution in the GM of 10YSZ starts to align along the $\langle 112 \rangle$ direction, in addition to the main $\langle 210 \rangle$ direction (Fig. 2). Since O_v diffusion must occur along the $\langle 110 \rangle$ direction to its 2NN position as required for the lowest energy pathway, the O_v diffusion in 10YSZ is expected to be restricted to few directions in order to avoid both the short contact between O_v (e.g., along $\langle 200 \rangle$) and the local formation of the Y– O_v pattern. Indeed, we found that the O_v diffusion to the 2NN position increases further the ordering of O_v along $\langle 112 \rangle$, but reduces the ordering of O_v along $\langle 210 \rangle$, as seen from Fig. 5. The more homogeneous distribution of O_v pushes effectively the Zr cations toward O_v sites (see Zr– O_v RDF in Fig. 5), leading to the energy increase in the FS.

IV. GENERAL DISCUSSIONS

A. Stability and structure of 8YSZ

Our convex hull results show that 8YSZ has a cubic phase as the GM, but is thermodynamically unstable and the degradation of 8YSZ into monoclinic (low Y) and cubic (high Y) phases is energetically favorable. The poor thermodynamics of 8YSZ confirms the previous suggestion by Predith *et al.*⁶⁴ based on DFT calculations for YSZ concentration from 12.3 mol. % to 80.2 mol. %. The monoclinic phases at 8YSZ itself is highly unstable, at least 29.8 meV per O above the GM [red dot in Fig. 1(a)], which suggests that the solid phase transition with only short-range Y diffusion is unlikely. We, therefore, expect that the slow solid-to-solid phase transition with the long-range Y migration is the main cause to the remarkable degradation in conductivity. This is supported by the experimental observations that tetragonal precipitates grow during the aging process from about 1 nm up to approximately 15 nm in 8YSZ at 950 °C.¹⁵ It should be mentioned that the monoclinic phase of 8YSZ is only more stable than the tetragonal phase at lower temperatures (<600 °C),⁷ and thus, the tetragonal phase is observed at the experiment temperature. On the other hand, our lowest energy pathways in bulk also demonstrate that the cation diffusion is unlikely kinetically due to too high energy barrier, which is consistent with the previous knowledge.^{65–67} The degradation of 8YSZ, thus, should initialize from surfaces and grain boundaries, which implies that the surface engineering is critical to stabilize 8YSZ.

Furthermore, our global PES data show that there are at least 6 minima energetically close (within 12 meV per O) to the GM (such as GM-1, Str-2, and Str-3), which implies that the GM configuration may not be the only structural pattern for 8YSZ under the working conditions, i.e., 1000 °C, but more likely as a mixture with many configurations, mainly differing in the Y–Y distributions. Indeed, from Boltzmann law and partition function, we can derive the occupancy rates of the low energy minima at experimental temperatures. The results show that the four low-lying structures (GM, Str-1, Str-2, and Str-3) have rather equal contribution (~12%) with the overall occupancy about ~50% in the total distribution. We, thus, conclude that the 8YSZ in reality should be best considered as a glass frozen at various local metastable configurations. Some experiments do support our conclusion. YSZ systems exhibit non-Arrhenius dependence of ionic conductivity with lower conductivity at high

temperatures. Ribes *et al.*⁶⁸ showed that this behavior is best fitted by the Vogel–Fulcher–Tammann equation of glassy kinetics, instead of the combination of Arrhenius equations of single or multiple diffusion processes/paths.^{62,63,68}

B. Conductivity mechanism of YSZ

Our results on the lowest energy pathways for O_v diffusion in 8YSZ and 10YSZ show that the individual O_v diffusion has the similar reaction barrier, ~1 eV, in the lowest energy pathway, which always moves along the $\langle 100 \rangle$ direction. No obvious preference is found for the diffusion over different cation–cation edges, i.e., Zr–Zr, Zr–Y (O_v is not near Y, and thus, no Y–Y edge diffusion channel is found). With the increase in Y concentration from 8 mol. % to 10 mol. %, we observe the O_v diffusion is limited to the 1NN position. This O anion migration picture could have profound implications on the conductivity mechanism of YSZ, as summarized below.

First, the O anion migration has to be coupled with each other and move sequentially. One individual O_v can only allow an O anion to diffuse to 1NN or 2NN position, which will immediately severely destabilize the system due to the unfavorable local structure pattern. The subsequent O anion movement has to occur at the other O_v sites, which, when completes, provides energetically more favorable structures. The cation movement in bulk is unlikely as no low energy pathways are found from the theory.

Second, the O anion diffusion barrier is rather constant, being ~1 eV and the local structural pattern can be either Y–O–Zr or Zr–O–Zr. The increase in Y concentrations will restrict the individual diffusion length for each O_v . The O_v diffusion length can be at least 3.6 Å to the 2NN position in 8YSZ, but is only 2.5 Å to the 1NN position in 10YSZ. This is the key reason why 8YSZ is better than other YSZ with higher Y concentrations.

The above mechanism explains the experimental observation by Kilo *et al.*,³⁴ who found that the apparent activation energy for O_v diffusion in YSZ with Y concentrations ranging from 8 mol. % to 24 mol. % at 650–1200 K was rather constant at ~1 eV, independent of the concentration. Overall, the low conductivity of YSZ with high Y concentrations can be attributed to the O_v aggregation along the $\langle 112 \rangle$ direction that limits significantly the diffusion length for each O_v diffusion. This effect is an entropy effect due to the configuration of O_v distribution in YSZ.

V. CONCLUDING REMARKS

By constructing the first Y–Zr–O ternary global NN potential and performing extensive SSW–NN global optimization, this work collects the global PES data for an important functional material, Y-stabilized ZrO₂, with Y₂O₃ ratio from 5.3 mol. % (Y₂Zr₁₈O₃₉) to 40 mol. % (Y₄Zr₃O₁₂). The Y–Zr–O G–NN is obtained by training 28 803 first principles global PES dataset and achieves the final accuracy of 7.674 meV/atom and 0.165 eV/Å for RMS energy and force, respectively. The 8YSZ is focused particularly because it achieves the highest conductivity for anion transportation but is not stable under working conditions. The thermodynamics stability and the kinetics of anion diffusion are determined for 8YSZ based on the structures and the lowest energy pathways from global PES exploration. Our main results are outlined as follows:

- (1) Only above 6.7 mol. % YSZ adopts the cubic lattice structure as the GM. 6.7YSZ, 20YSZ, and 40YSZ are three thermodynamic stable phases, which are monoclinic, cubic, and cubic lattice structures, respectively.
- (2) O_v prefers to locate near Zr cation (1NN position) in general, and only above 33.3% O_v can appear near Y as the 1NN in the GM structure.
- (3) 8YSZ is thermodynamically unstable, and the phase segregation into the 6.7YSZ and 20YSZ is exothermic by 12 meV per O atom. In the GM of 8YSZ, Y cations tend to be paired, forming the Y–O–Y local structure pattern: the homogeneous distribution of Y cations is less favorable by at least 6.5 meV per O atom.
- (4) The O_v distribution in 8YSZ differs from that in other cubic YSZs with higher Y concentrations. The O_v aligns along $\langle 210 \rangle$ and $\langle 222 \rangle$ in 8YSZ, but the O_v alignment along $\langle 112 \rangle$ is a major feature in other YSZs.
- (5) The O anion diffusion is mediated by O_v and always along the $\langle 100 \rangle$ direction in the lowest energy pathway. The reaction barrier is ~ 1 eV for both 8YSZ and 10YSZ, but the diffusion distance is longer, being 3.6 Å for 8YSZ and only 2.5 Å for 10YSZ. This difference is attributed to the presence of O_v aggregation along the $\langle 112 \rangle$ direction in 10YSZ that hinders the O anion diffusion. The conductivity is, thus, expected to be achieved via coupled O anion movement under working conditions, as also suggested previously,^{30,31} where multiple O anions near different O_v diffuse sequentially.

SUPPLEMENTARY MATERIAL

See the [supplementary material](#) for construction of the Y–Zr–O ternary G–NN potential; definition of distance-weighted Steinhart order parameter; benchmark of G–NN potential against DFT calculations; automated SSW–RS to search for anion diffusion pathways; supercells utilized in SSW global optimization and the representative structures in 8YSZ; RDFs of cation–O pair for GMs of YSZs at different concentrations; RDF of cation– O_v , O_v – O_v , and Y–Y pairs for four low-lying minima in 8YSZ; and XYZ coordination of all GM structures and the anion diffusion pathway of 8YSZ

ACKNOWLEDGMENTS

This work was supported by the National Key Research and Development Program of China (Grant No. 2018YFA0208600) and the National Science Foundation of China (Grant Nos. 21533001 and 91745201).

REFERENCES

- ¹E. Ryshkewitch, *Oxide Ceramics: Physical Chemistry and Technology* (Academic Press, New York, NY, 1960), p. 350.
- ²S. Fabris, A. T. Paxton, and M. W. Finnis, “A stabilization mechanism of zirconia based on oxygen vacancies only,” *Acta Mater.* **50**, 5171–5178 (2002).
- ³A. Chronos, B. Yildiz, A. Tarancón, D. Parfitt, and J. A. Kilner, “Oxygen diffusion in solid oxide fuel cell cathode and electrolyte materials: Mechanistic insights from atomistic simulations,” *Energy Environ. Sci.* **4**(8), 2774–2789 (2011).
- ⁴K. Knipe, A. Manero, S. F. Siddiqui, C. Meid, J. Wischek, J. Okasinski, J. Almer, A. M. Karlsson, M. Bartsch, and S. Raghavan, “Strain response of thermal barrier coatings captured under extreme engine environments through synchrotron X-ray diffraction,” *Nat. Commun.* **5**, 4559 (2014).
- ⁵R. C. Garvie, R. H. Hannink, and R. T. Pascoe, “Ceramic steel?,” *Nature* **258**, 703–704 (1970).
- ⁶M. Jaipal and A. Chatterjee, “Relative occurrence of oxygen-vacancy pairs in Yttrium-containing environments of Y_2O_3 -doped ZrO_2 can be crucial to ionic conductivity,” *J. Phys. Chem. C* **121**(27), 14534–14543 (2017).
- ⁷Y. Suzuki, “Phase transition temperature of fluorite-type ZrO_2 - Y_2O_3 solid solutions containing 8–44 mol% Y_2O_3 ,” *Solid State Ionics* **81**, 211–216 (1995).
- ⁸J. Chevalier, L. Gremillard, A. V. Virkar, and D. R. Clarke, “The tetragonal-monoclinic transformation in zirconia: Lessons learned and future trends,” *J. Am. Ceram. Soc.* **92**(9), 1901–1920 (2009).
- ⁹S. Hull, “Superionics: Crystal structures and conduction processes,” *Rep. Prog. Phys.* **67**(7), 1233–1314 (2004).
- ¹⁰N. Mahato, A. Banerjee, A. Gupta, S. Omar, and K. Balani, “Progress in material selection for solid oxide fuel cell technology: A review,” *Prog. Mater. Sci.* **72**, 141–337 (2015).
- ¹¹R. E. W. Casselton, “Low field DC conduction in Yttria-stabilized zirconia,” *Phys. Status Solidi A* **2**, 571–585 (1970).
- ¹²T. H. Etsell and S. N. Flengas, “Electrical properties of solid oxide electrolytes,” *Chem. Rev.* **70**, 339–376 (1970).
- ¹³M. Rühle, “Microscopy of structural ceramics,” *Adv. Mater.* **9**(3), 195–217 (1997).
- ¹⁴O. Yamamoto, Y. Arachi, H. Sakai, Y. Takeda, N. Imanishi, Y. Mizutani, M. Kawai, and Y. Nakamura, “Zirconia based oxide ion conductors for solid oxide fuel cells,” *Ionics* **4**, 403–407 (1998).
- ¹⁵B. Butz, P. Kruse, H. Stormer, D. Gerthsen, A. Muller, A. Weber, and E. Iverstiffe, “Correlation between microstructure and degradation in conductivity for cubic Y_2O_3 -doped ZrO_2 ,” *Solid State Ionics* **177**(37–38), 3275–3284 (2006).
- ¹⁶F. T. Ciacchi and S. P. S. Badwal, “The system Y_2O_3 - Sc_2O_3 - ZrO_2 : Ionic conductivity studies,” *J. Eur. Ceram. Soc.* **7**, 197–206 (1991).
- ¹⁷M. Hattori, Y. Takeda, J. H. Lee, S. Ohara, K. Mukai, T. Fukui, S. Takahashi, Y. Sakaki, and A. Nakanishi, “Effect of annealing on the electrical conductivity of the Y_2O_3 - ZrO_2 system,” *J. Power Sources* **131**(1–2), 247–250 (2004).
- ¹⁸B. Butz, R. Schneider, D. Gerthsen, M. Schowalter, and A. Rosenauer, “Decomposition of 8.5mol.% Y_2O_3 -doped zirconia and its contribution to the degradation of ionic conductivity,” *Acta Mater.* **57**(18), 5480–5490 (2009).
- ¹⁹D. Steele and B. E. F. Fender, “The structure of cubic $ZrO_2:YO_{1.5}$ solid solutions by neutron scattering,” *J. Phys. C: Solid State Phys.* **7**, 1–11 (1974).
- ²⁰M. Morinaga, J. B. Cohen, and J. F. Jnr, “X-ray diffraction study of $Zr(Ca,Y)O_{2-x}$: I. The average structure,” *Acta Crystallogr., Sect. A: Cryst. Phys., Diff., Theor. Gen. Crystallogr.* **35**, 789–795 (1979).
- ²¹M. Morinaga, J. B. Cohen, and J. F. Jnr, “X-ray diffraction study of $Zr(Ca,Y)O_{2-x}$: II. Local ionic arrangements,” *Acta Crystallogr., Sect. A: Cryst. Phys., Diff., Theor. Gen. Crystallogr.* **36**, 520–530 (1980).
- ²²C. R. A. Catlow, A. V. Chadwick, G. N. Greaves, and L. M. Moroney, “EXAFS study of Yttria-stabilized zirconia,” *J. Am. Ceram. Soc.* **69**(3), 272–277 (1986).
- ²³B. W. Veal, A. G. McKale, A. P. Paulikas, S. J. Rothman, and L. J. Nowicki, “EXAFS study of Yttria stabilized zirconia,” *Physica B+C* **150**, 234–240 (1988).
- ²⁴P. Li and J. E. Penner-Hahn, “X-ray-absorption studies of zirconia polymorphs. II. Effect of Y_2O_3 dopant on ZrO_2 structure,” *Phys. Rev. B* **48**, 10074–10081 (1993).
- ²⁵A. Bogicevic and C. Wolverton, “Nature and strength of defect interactions in cubic stabilized zirconia,” *Phys. Rev. B* **67**(2), 024106–024113 (2003).
- ²⁶X. Xia, R. Oldman, and R. Catlow, “Computational modeling study of bulk and surface of Yttria-stabilized cubic zirconia,” *Chem. Mater.* **21**(15), 3576–3585 (2009).
- ²⁷G. Stapper, M. Bernasconi, N. Nicoloso, and M. Parrinello, “Ab initio study of structural and electronic properties of Yttria stabilized cubic zirconia,” *Phys. Rev. B* **59**(2), 797–810 (1999).
- ²⁸K. Kawata, H. Maekawa, T. Nemoto, and T. Yamamura, “Local structure analysis of YSZ by Y-89 MAS-NMR,” *Solid State Ionics* **177**(19–25), 1687–1690 (2006).

- ²⁹J. P. Goff, W. Hayes, S. Hull, M. T. Hutchings, and K. N. Clausen, "Defect structure of Yttria-stabilized zirconia and its influence on the ionic conductivity at elevated temperatures," *Phys. Rev. B* **59** (22), 14202–14219 (1999).
- ³⁰F. Pietrucci, M. Bernasconi, A. Laio, and M. Parrinello, "Vacancy-vacancy interaction and oxygen diffusion in stabilized cubic ZrO₂ from first principles," *Phys. Rev. B* **78**(9), 094301–094307 (2008).
- ³¹D. Marrocchelli, P. A. Madden, S. T. Norberg, and S. Hull, "Structural disorder in doped zirconias, Part II: Vacancy ordering effects and the conductivity maximum," *Chem. Mater.* **23**, 1365–1373 (2011).
- ³²F. Shimojo, T. Okabe, F. Tachibana, M. Kobayashi, and H. Okazaki, "Molecular dynamics studies of Yttria stabilized zirconia. I. Structure and oxygen diffusion," *J. Phys. Soc. Jpn.* **61**, 2848–2857 (1992).
- ³³R. Krishnamurthy, Y. G. Yoon, D. J. Srolovitz, and R. Car, "Oxygen diffusion in Yttria stabilized zirconia: A new simulation model," *J. Am. Ceram. Soc.* **87**(10), 1821–1830 (2004).
- ³⁴M. Kilo, C. Argirusis, G. Borchardt, and R. A. Jackson, "Oxygen diffusion in Yttria stabilised zirconia—experimental results and molecular dynamics calculations," *Phys. Chem. Chem. Phys.* **5**(11), 2219–2224 (2003).
- ³⁵M. Asadikiya and Y. Zhong, "Oxygen ion mobility and conductivity prediction in cubic Yttria-stabilized zirconia single crystals," *J. Mater. Sci.* **53**(3), 1699–1709 (2017).
- ³⁶R. Pornprasertsuk, P. Ramanarayanan, C. B. Musgrave, and F. B. Prinz, "Predicting ionic conductivity of solid oxide fuel cell electrolyte from first principles," *J. Appl. Phys.* **99**, 103513–103521 (2005).
- ³⁷H. C. Huang, P. C. Su, S. K. Kwak, R. Pornprasertsuk, and Y. J. Yoon, "Molecular dynamics simulation of oxygen ion diffusion in Yttria stabilized zirconia single crystals and bicrystals," *Fuel Cells* **14**(4), 574–580 (2014).
- ³⁸J. Kondoh, S. Kikuchi, Y. Tomii, and Y. Ito, "Effect of aging on Yttria stabilized zirconia: III. A study of the effect of local structures on conductivity," *J. Electrochem. Soc.* **145**(5), 1550–1560 (1998).
- ³⁹J. Kondoh, T. Kawashima, S. Kikuchi, Y. Tomii, and Y. Ito, "Effect of aging on Yttria-stabilized zirconia I. A study of its electrochemical properties," *J. Electrochem. Soc.* **145**(5), 1527–1536 (1998).
- ⁴⁰J. Kondoh, T. Kawashima, S. Kikuchi, Y. Tomii, and Y. Ito, "Effect of aging on Yttria-stabilized zirconia II. A study of the effect of the microstructure on conductivity," *J. Electrochem. Soc.* **145**(5), 1536–1550 (1998).
- ⁴¹W. C. Mackrodt and P. M. Woodrow, "Theoretical estimates of point defect energies in cubic zirconia," *J. Am. Ceram. Soc.* **69**, 277–280 (1986).
- ⁴²P. K. Schelling, S. R. Phillpot, and D. Wolf, "Mechanism of the cubic-to tetragonal phase transition in zirconia and Yttria-stabilized zirconia by molecular-dynamics simulation," *J. Am. Ceram. Soc.* **84**(7), 1609–1619 (2001).
- ⁴³M. Kilo, "Modeling of cation diffusion in oxygen ion conductors using molecular dynamics," *Solid State Ionics* **175**(1–4), 823–827 (2004).
- ⁴⁴R. Devanathan, W. Weber, S. Singhal, and J. Gale, "Computer simulation of defects and oxygen transport in Yttria-stabilized zirconia," *Solid State Ionics* **177**(15–16), 1251–1258 (2006).
- ⁴⁵W. Araki and Y. Arai, "Molecular dynamics study on oxygen diffusion in Yttria-stabilized zirconia subjected to uniaxial stress in terms of Yttria concentration and stress direction," *Solid State Ionics* **181**(33–34), 1534–1541 (2010).
- ⁴⁶V. V. Sizov, M. J. Lampinen, and A. Laaksonen, "Molecular dynamics simulation of oxygen diffusion in cubic Yttria-stabilized zirconia: Effects of temperature and composition," *Solid State Ionics* **266**, 29–35 (2014).
- ⁴⁷C. Shang and Z.-P. Liu, "Stochastic surface walking method for structure prediction and pathway searching," *J. Chem. Theory Comput.* **9**(3), 1838–1845 (2013).
- ⁴⁸C. Shang, X.-J. Zhang, and Z.-P. Liu, "Stochastic surface walking method for crystal structure and phase transition pathway prediction," *Phys. Chem. Chem. Phys.* **16**(33), 17845–17856 (2014).
- ⁴⁹S.-D. Huang, C. Shang, X.-J. Zhang, and Z.-P. Liu, "Material discovery by combining stochastic surface walking global optimization with a neural network," *Chem. Sci.* **8**(9), 6327–6337 (2017).
- ⁵⁰S.-D. Huang, C. Shang, P.-L. Kang, and Z.-P. Liu, "Atomic structure of boron resolved using machine learning and global sampling," *Chem. Sci.* **9**(46), 8644–8655 (2018).
- ⁵¹S. Ma, S.-D. Huang, and Z.-P. Liu, "Dynamic coordination of cations and catalytic selectivity on zinc–chromium oxide alloys during syngas conversion," *Nat. Catal.* **2**(8), 671–677 (2019).
- ⁵²S.-D. Huang, C. Shang, P.-L. Kang, X.-J. Zhang, and Z.-P. Liu, "LASP: Fast global potential energy surface exploration," *Wiley Interdiscip. Rev.: Comput. Mol. Sci.* **9**, e1415 (2019).
- ⁵³G. Kresse and J. Furthmüller, "Efficiency of *ab-initio* total energy calculations for metals and semiconductors using a plane-wave basis set," *Comput. Mater. Sci.* **6**(1), 15–50 (1996).
- ⁵⁴S. Ma, C. Shang, and Z.-P. Liu, "Heterogeneous catalysis from structure to activity via SSW-NN method," *J. Chem. Phys.* **151**(5), 050901 (2019).
- ⁵⁵J. P. Perdew, K. Burke, and M. Ernzerhof, "Generalized gradient approximation made simple," *Phys. Rev. Lett.* **77**(18), 3865–3868 (1996).
- ⁵⁶G. Kresse and D. Joubert, "From ultrasoft pseudopotentials to the projector augmented-wave method," *Phys. Rev. B* **59**(3), 1758–1775 (1999).
- ⁵⁷H. J. Monkhorst and J. D. Pack, "Special points for Brillouin-zone integrations," *Phys. Rev. B* **13**(12), 5188–5192 (1976).
- ⁵⁸X.-J. Zhang, C. Shang, and Z.-P. Liu, "Double-ended surface walking method for pathway building and transition state location of complex reactions," *J. Chem. Theory Comput.* **9**(12), 5745–5753 (2013).
- ⁵⁹C. Shang and Z.-P. Liu, "Constrained broyden dimer method with bias potential for exploring potential energy surface of multistep reaction process," *J. Chem. Theory Comput.* **8**(7), 2215–2222 (2012).
- ⁶⁰C. Gonzalez and H. B. Schlegel, "Reaction path following in mass-weighted internal coordinates," *J. Phys. Chem.* **94**(14), 5523–5527 (1990).
- ⁶¹X.-J. Zhang, C. Shang, and Z.-P. Liu, "Pressure-induced silica quartz amorphization studied by iterative stochastic surface walking reaction sampling," *Phys. Chem. Chem. Phys.* **19**(6), 4725–4733 (2017).
- ⁶²Y. Li, J. H. Gong, Y. S. Xie, and Y. F. Chen, "Analysis of non-linear Arrhenius behavior of ionic conduction in cubic zirconia stabilized with Yttria and calcia," *J. Mater. Sci. Lett.* **21**, 157–159 (2002).
- ⁶³K. L. Ngai, "Evidence of interaction between oxygen ions from conductivity relaxation and quasielastic light scattering data of Yttria-stabilized zirconia," *Philos. Mag. B* **77**, 187–195 (1998).
- ⁶⁴A. Predith, G. Ceder, C. Wolverton, K. Persson, and T. Mueller, "Ab initio prediction of ordered ground-state structures in ZrO₂-Y₂O₃," *Phys. Rev. B* **77**(14), 144104–144107 (2008).
- ⁶⁵M. Kilo, R. A. Jackson, and G. Borchardt, "Computer modelling of ion migration in zirconia," *Philos. Mag. B* **83**(29), 3309–3325 (2003).
- ⁶⁶M. Kilo, "Cation transport in stabilised zirconias," *Defect Diffus. Forum* **242–244**, 185–254 (2005).
- ⁶⁷Y. Dong, L. Qi, J. Li, and I. W. Chen, "A computational study of Yttria-stabilized zirconia: II. Cation diffusion," *Acta Mater.* **126**, 438–450 (2017).
- ⁶⁸M. Ribes, G. Taillades, and A. Pradel, "Non-Arrhenius conductivity in glassy and crystallized fast ion conductors: A manifestation of cationic disorder," *Solid State Ionics* **105**, 159–165 (1998).